Long-Time Molecular Motions and Local Chain Dynamics in n-$C_{44}H_{90}$ Melts by Molecular Dynamics Simulations

Grant D. Smith[1]

Thermosciences Institute, STC 230-3 NASA Ames Research Center, Moffett Field, California 94035

Do Y. Yoon*

IBM Research Division, Almaden Research Center, 650 Harry Road, San Jose, California 95120

Richard L. Jaffe

NASA Ames Research Center, Moffett Field, California 94035

Received November 22, 1994; Revised Manuscript Received April 6, 1995[⊗]

ABSTRACT: Dynamic properties of n-$C_{44}H_{90}$ melts have been investigated via molecular dynamics simulations with emphasis on long-time molecular motions and their connection to local chain dynamics. Correlation of conformational transitions is also examined. The model employs an atomistic force field which includes hydrogen atoms explicitly and reproduces the conformational energy surface of n-butane and n-hexane, in good agreement with recent ab initio electronic structure calculations. The simulations yield self-diffusion coefficients which are in good agreement with experiment. However, the monomer friction constants calculated from the self-diffusion coefficients are considerably smaller than estimates from the Rouse model fit of the end-to-end chain vector reorientation and experimental melt viscosities, indicative of the fact that these chains are not long enough to assume Gaussian coils. The local bond vector orientation autocorrelation functions (OACF) exhibit important contributions from long relaxation time modes, resulting in long-time "tails" in the OACF. In these cases the OACF can be accurately described only by empirical functions and theoretical models which account for the long relaxation time modes. Relaxation times of the long-time tails for the local bond vector OACF approach those of the end-to-end vector OACF of the $C_{44}H_{90}$ chains and are due to correlation of the relaxation of the local bond vectors to the relaxation of the chain backbone vectors. The torsional autocorrelation functions also show a long-time component which can be described reasonably by exponential-like decay. The relaxation times for the long-time component of the torsional autocorrelation functions are much shorter than was found for the long-time modes of bond vector OACF, indicative of local dynamic heterogeneities. For conformational transitions, directly correlated transitions are found to occur for the self, second, and fourth neighbors. Moreover, the second-neighbor correlated transitions appear to propagate more or less randomly along the chain.

Introduction

In a recent paper,[2] we compared in detail the rates of local chain dynamics in n-$C_{44}H_{90}$ melts as determined from molecular dynamics simulation with results of experimental ^{13}C NMR relaxation studies. We found that our model, which includes hydrogen atoms explicitly, gives good agreement with the experimental spin−lattice relaxation time (T_1) and nuclear Overhauser enhancement (NOE) values. In this paper, we continue the study of the dynamic properties of n-$C_{44}H_{90}$ melts by considering in detail long-time molecular motions and their connection to local chain dynamics. As part of the discussion of local chain dynamics and as a follow-up to our recent paper,[2] we also consider correlation of conformational transitions in n-$C_{44}H_{90}$ melts.

Force Field and Simulation Methodology

The explicit atom force field used in the simulations is described in detail elsewhere.[3] A survey of the recent literature discussed in ref 4 reveals that there remains some question as to the shape of the conformational energy surface for rotations about the C−C−C−C torsion in n-alkanes. A major discrepancy in the potentials lies in the value of the cis barrier. Some experimental studies suggest that the g^+-g^- (cis) barrier is comparable to the $g-t$ barrier, while other experimental studies and quantum chemistry calculations suggest it is much higher.[4] Here, t is the trans conformation and $g^\pm$ the gauche conformations. The implications of this uncertainty in the cis barrier on conformational dynamics are considerable: if the cis barrier is comparable to the $g-t$ barrier, $g^+ \rightleftharpoons g^-$ transitions will occur rapidly, while a high barrier would make these transitions unimportant compared to $t \rightleftharpoons g^\pm$ transitions. In order to better understand the conformational energy surface for n-alkanes, we have recently conducted an extensive ab initio electronic structure study of the conformational energies of n-butane and n-hexane. The results will be presented in detail elsewhere.[4] Selected results of our ab initio study are summarized in Table 1.

In our study, geometry optimizations for n-butane were performed at the MP2 level of electron correlation with a 6-311G(2df,p) basis set. This is a valence triple-ζ basis set with two sets of d polarization functions and a set of f polarization functions on the carbon atoms and a set of p polarization functions on the hydrogen atoms. The resulting C−C−C−C torsional angles for the t and g conformations along with the $t-g$ and cis saddle points

[⊗] Abstract published in *Advance ACS Abstracts,* July 1, 1995.

0024-9297/95/2228-5897$09.00/0

Table 1. Conformational Geometries and Energies of *n*-Butane and *n*-Hexane

conformation	geometry: basis set	geometry: torsional angle (deg)	energy (kcal/mol): basis set	SCF	MP2	CCSD	CCSD(T)
		Gauche Energy					
butane *g*	6-311G** MP2	117.8	6-311G**	1.05	0.51	0.59	0.54
hexane *g*	6-311G** MP2	117.8	6-311G**	1.17	0.44		
butane *g*	6-311G(2df,p) MP2	117.2	6-311G(2df,p)	1.09	0.53	0.62	
butane *g*	6-311G(2df,p) MP2	117.2	cc-pVTZ	1.13	0.56	0.65	0.59
		t−*g* Barrier Energy					
butane *t*−*g*	6-311G** MP2	60.7	6-311G**	3.68	3.40	3.33	3.28
hexane *t*−*g*	6-311G** MP2	60.5	6-311G**	3.36	2.89		
butane *t*−*g*	6-311G(2df,p) MP2	60.5	6-311G(2df,p)	3.69	3.45	3.36	
butane *t*−*g*	6-311G(2df,p) MP2	60.5	cc-pVTZ	3.67	3.44	3.36	3.31
		Cis Energy					
butane cis	6-311G** MP2	180.0	6-311G**	6.36	5.92	5.79	5.74
hexane cis	6-311G** MP2	180.0	6-311G**	6.48	5.63		
butane cis	6-311G(2df,p) MP2	180.0	6-311G(2df,p)	6.37	5.76	5.67	
butane cis	(6-311G(2df,p) MP2	180.0	cc-pVTZ	6.39	5.67	5.58	5.48

are given in Table 1. Energies of these conformations, relative to the *t* conformation, were also determined using a correlation-consistent valence triple-ζ basis set with poalrization functions (cc-pVTZ),[5] of the form [4s3p2df/3s2p], employing the 6-311G(2df,p) MP2 optimized geometries. The SCF, MP2, CCSD,[6] and CCSD(T)[6] (coupled-cluster with single, double, and triple excitations) energies are given in Table 1. The largest basis set and best electron correlation treatment used (cc-pVTZ, CCSD(T)) represent a considerable improvement over previous calculations. We believe that further improvements in basis set or electron correlation treatment are unlikely to significantly change these energies.[4] As can be seen from Table 1, the cis barrier in *n*-butane is much higher than the *t*−*g* barrier. Conformational energies for the central torsion in *n*-hexane were also investigated. When compared to those of *n*-butane from the same basis set and electron correlation (6-311G**, MP2), the *n*-hexane energies showed a slight lowering of the *g* energy (<0.1 kcal/mol), while the *t*−*g* barrier was found to be about 0.5 kcal/mol lower in *n*-hexane.[4] Only a small lowering of the cis barrier was seen (0.3 kcal/mol). Our force field[3] potential yields, relative to *t*, a *g* energy of 0.48 kcal/mol, a *t*−*g* barrier of 3.0 kcal/mol, and a cis energy of 4.8 kcal/mol for *n*-butane, in good agreement with the ab initio predictions. The cis barrier is high enough to preclude most $g^+ \rightleftarrows g^-$ transitions (see below).

The simulations were performed at constant temperature and volume using molecular dynamics algorithms described elsewhere.[2,3] After equilibration, the total sampling time was approximately 1.1 ns at 450 K and 1.4 ns at 400 K. Simulations of isolated chains, where all intramolecular interactions were considered but intermolecular interactions were not, were performed at 400 K. For these simulations, the total sampling time was 1.4 ns.

Results and Discussion

End-to-End Vector Reorientation and Self-Diffusion Coefficient. The end-to-end vector orientation autocorrelation functions (end-to-end OACF) $P_1(t)$ and $P_2(t)$ for *n*-$C_{44}H_{90}$ at 400 and 450 K are shown in Figure 1. The OACF for a given unit vector **n** are defined as

$$P_1(t) = \langle \mathbf{n}(t)\cdot\mathbf{n}(0)\rangle \tag{1}$$

$$P_2(t) = \frac{3\langle[\mathbf{n}(t)\cdot\mathbf{n}(0)]^2\rangle - 1}{2} \tag{2}$$

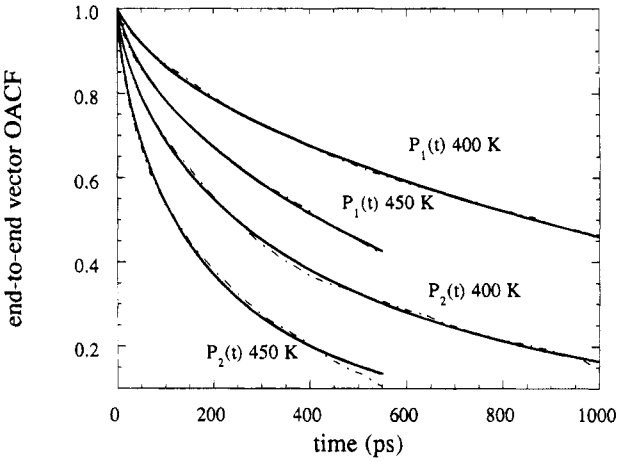

Figure 1. End-to-end vector autocorrelation functions. Simulation data are dash−dot lines. Solid lines are KWW fits for $P_2(t)$ data and fits of eq 3 for $P_1(t)$ data.

Rouse relaxation times τ_R were determined by fitting the equation[7]

$$P_1(t) = a \sum_{p=1}^{n(\text{odd})} \frac{\exp(-p^2 t/\tau_R)}{p^2} \tag{3}$$

where *p* is the order of the Rouse mode, *n* is the highest order mode considered, and *a* is the normalization factor. The fit was not improved for $n > 7$. The resulting fits, which are quite good, are shown in Figure 1. The Rouse times are given in Table 2. The end-to-end OACF were also fit with the Kohlrausch−Williams−Watts (KWW) equation

$$P(t) = \exp[-(t/\tau)^\beta] \tag{4}$$

The resulting parameters are also given in Table 2. The fits of eq 4 to the $P_2(t)$ autocorrelation functions are shown in Figure 1. The fit is reasonable, with the largest variations occurring at long times.

The mean-square displacements of the chain centers of mass as a function of time is shown in Figure 2. From the slopes of these curves, self-diffusion coefficients D_N can be extracted. The values are given in Table 2. As the total mean-square displacement at 400 K is only slightly greater than one mean-square radius of gyration, the uncertainty in the calculated self-diffusion coefficient is estimated to be ±25%, while the uncertainty at 450 K is estimated to be ±10%. Experimental values of the self-diffusion coefficient in $C_{44}H_{90}$ melts[8]

Table 2. End-to-End Vector Reorientation Times, Self-Diffusion Coefficients, and Monomer Friction Constants

		τ_{KWW} (ps)		β		D_N (10^{-6} cm^2/s)		monomer friction constant (10^{-10} dyn s/cm)		
temp (K)	τ_R (ps)	$P_1(t)$	$P_2(t)$	$P_1(t)$	$P_2(t)$	simulation	exp[a]	$\zeta(D_N)$[b]	$\zeta(\tau_R)$	$\zeta(\eta)$[c]
400	1614	1436	423	0.73	0.69	1.9 ± 0.5	2.4	6.6 (5.2)	8.1	10.1
450	791	701	202	0.73	0.69	5.4 ± 0.6	4.9	2.6 (2.9)	4.6	5.8

[a] Estimated from the temperature dependence of the monomer friction factor, using the experimental value of 4.8×10^{-6} cm^2/s at 448 K as a basis (from ref 8). [b] Numbers in parentheses were determined using eq 5 with the experimental self-diffusion coefficients. [c] From experimentally measured viscosities (ref 8).

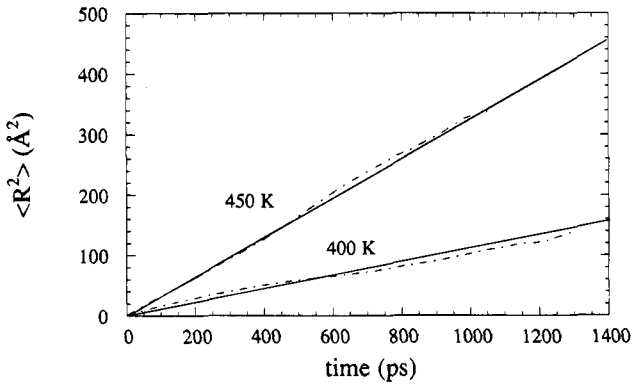

Figure 2. Mean-square chain center of mass displacement as a function of time. Simulation data are dash–dot lines. Self-diffusion coefficients were determined from the slopes of the solid lines.

are shown in Table 2. Our values from simulation are in good agreement with experiment given the uncertainty in the simulated values as discussed above.

For polymer melts without entanglements, it is possible to calculate a monomer friction factor based upon the self-diffusion coefficient[7]

$$\zeta(D_N) = \frac{k_B T}{N D_N} \tag{5}$$

and based upon the Rouse model[7]

$$\zeta(\tau_R) = \frac{3\pi^2 k_B T \tau_R}{N\langle R^2\rangle} \tag{6}$$

where N is the number of monomer units and $\langle R^2\rangle$ is the mean-square end-to-end distance. The resulting monomer friction factors are given in Table 2. The differences between the values obtained from eq 5 and 6 are greater than the estimated uncertainty in the values. The discrepancy indicates that the n-$C_{44}H_{90}$ chain is not long enough, compared with its persistence length,[9] to exhibit Gaussian coil characteristics as assumed by the Rouse model. In contrast, preliminary analysis of molecular dynamics simulations of n-$C_{100}H_{202}$ melts[10] indicates that this discrepancy seems to disappear for the long chains, consistent with the configurational characteristics of polymethylene.[9]

In the Rouse model, the monomer friction constant can also be determined from the melt viscosity.[7] These values, labeled $\zeta(\eta)$, based upon experimental viscosities,[8] are shown in Table 2. The discrepancy between these values and the $\zeta(D_N)$ values based upon experimental self-diffusion coefficients is a further indication that the chains are not Gaussian coils. On the other hand, the values of $\zeta(\tau_R)$ as measured from simulation, including temperature dependence, are in good agreement with that of $\zeta(\eta)$ as determined from experiment. The temperature dependence of $\zeta(D_N)$ does not agree as well with experiment, probably due to the large uncertainty in D_N at 400 K as discussed above.

Bond Vector Orientational Autocorrelation Functions. Previously,[2] we investigated the behavior of the C–H vector $P_2(t)$ OACF and found that $P_2(t)$ for C–H vectors for the chain end carbons could be fit quite well by the KWW equation. However, the KWW equation failed to describe the $P_2(t)$ OACF for C–H vectors for the interior carbons at long times.

Many theoretical models for the OACF exist in the literature. For the purpose of gaining a better understanding of the bond vector OACF, but not to validate any particular model, we have chosen to investigate the ability of two of these models to represent the bond vector OACF obtained from simulation. Specifically, these are the Hall–Helfand (HH) model[11,12] and the Valeur–Jarry–Geny–Monnerie (VJGM) model.[13] In addition, we will discuss fitting the OACF with the empirical KWW equation.

Analytical Models. The two analytical models (HH and VJGM) we consider are fundamentally different. The HH model was derived to represent conformational (torsional) autocorrelation functions by considering single transitions and correlated pair transitions, and is given by

$$P(t) = [\exp(-t/\tau_0)][\exp(-t/\tau_1) I_0(t/\tau_1)] \tag{7}$$

where I_0 is the zeroth-order modified Bessel function. Single transitions lead to the τ_0 term, while the τ_1 term is a diffusion term related to the correlated pair transitions. By definition, the conformational autocorrelation function decays entirely by conformational transitions. Hence, the HH model does not include contributions from long-wavelength modes which may contribute to bond vector OACF.[12] In order to describe this long-time behavior, a single exponential term with a relaxation time we label here τ_{tail} was included, yielding an equation of the form[12]

$$P(t) = A \exp(-t/\tau_0) \exp(-t/\tau_1) I_0(t/\tau_1) + (1 - A) \exp(-t/\tau_{tail}) \tag{8}$$

This form of the HH model is identical to the DLM model.[14] In the DLM model, the relaxation time for the single exponential is shorter than τ_1, as in this model the single exponential term was added to the HH model to describe effects of short relaxation time librational motions.

In the VJGM model, the OACF is given by

$$P(t) = \exp(t/\tau_1) \operatorname{erfc}[(t/\tau_1)^{1/2}] \tag{9}$$

This describes the behavior of an infinite chain on a tetrahedral lattice undergoing elementary three-bond jumps. The relaxation time τ_1 is related to the conformational jump frequency. The model includes contributions from long wavelength or relaxation time modes

Table 3. $P_1(t)$ Autocorrelation Function Fit Parameters

model	temp (K)	τ (ps)	τ_0 (ps)	τ_1 (ps)	τ_{tail} (ps)	β	A
			C−C Vector				
MKWW	400	13.2			953	0.56	0.64
HH			184	9.7	1016		0.65
VJGM				70.0			
MKWW	450	9.6			550	0.47	0.72
HH			120	5.8	462		0.70
VJGM				25.2			
			C−C−C Chord Vector[a]				
MKWW	400	30.8			916	0.50	0.542
VJGM				145.8			
MKWW	450	20.8			545	0.47	0.623
VJGM				63.6			
			C−H Vector				
MKWW	400	8.0			1004	0.70	0.996
MKWW	450	4.5			500[b]	0.72	0.996[b]

[a] See Figure 4 for definition. [b] The autocorrelation function was fit equally well by $A = 0.994$ and $\tau_{tail} = 115$ ps.

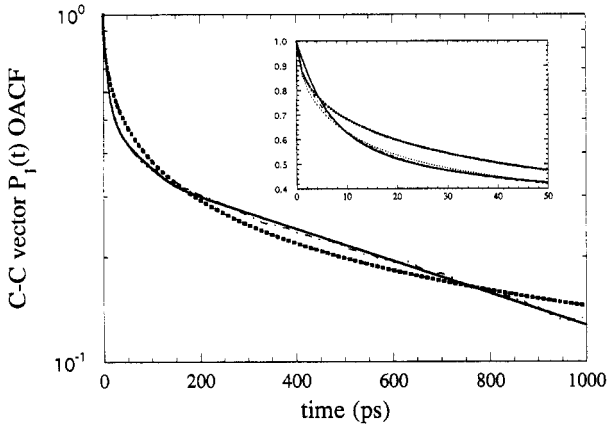

Figure 3. $P_1(t)$ OACF for the C−C bond vector at 400 K. Simulation data are the dash−dot line. The dotted line is the fit of the MKWW model, the solid line the HH model, and the heavy dotted line the VJGM model. The inset shows short-time behavior. The HH and MKWW fits are distinguishable only in the inset plot.

and yields a $1/t^{1/2}$ dependence of $P(t)$ at long times. We have also fit the OACF by the equation

$$P(t) = A \exp[-(t/\tau)^{\beta}] + (1 - A) \exp(-t/\tau_{tail}) \quad (10)$$

Equation 10 is the KWW equation (eq 4) with an additional single exponential term to describe long-time behavior. We refer to this equation as the modified KWW (MKWW) equation. For all OACF, the values from simulations are averages over vectors involving the central carbons (5−40) of n-$C_{44}H_{90}$.

***P*$_1$*(t)* Autocorrelation Functions.** The C−C vector $P_1(t)$ OACF for n-$C_{44}H_{90}$ melts at 400 and 450 K were fit by the HH (with single long relaxation time exponential), VJGM, and MKWW models. Data up to 1.0 and 0.7 ns were used in fitting the bond vector OACF at 400 and 450 K, respectively, except in cases where the OACF would go negative at time shorter than these limits. In these cases, data up to the time when the OACF first goes negative were used in fitting the OACF. The resulting parameters are given in Table 3. The fits at 400 K are shown in Figure 3. The many-parameter HH and MKWW models fit the C−C $P_1(t)$ OACF quite well. Parameters for the long-time single exponential term are quite similar for both fits. This term accounts for 30−40% of the relaxation of the $P_1(t)$ OACF for the C−C vector. In contrast to the HH model, the DLM model was not able to fit the data well. This indicates

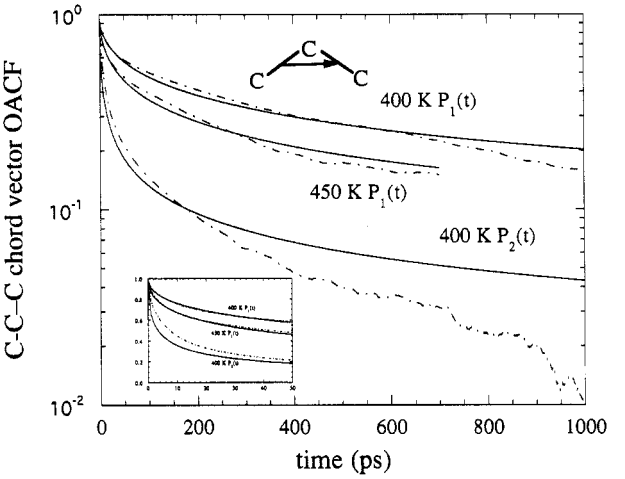

Figure 4. OACF for the C−C−C chord vector (as shown). Simulation data are the dash−dot lines. The solid lines are fits of the VJGM model. The inset shows short-time behavior.

the importance of contributions of the long relaxation time modes to the OACF.

Figure 3 reveals that the fit of the VJGM to the C−C $P_1(t)$ OACF is poorer than that obtained from the HH and MKWW models, but it should be noted that there is only a single adjustable parameter in the VJGM model. The fit of this function to the C−C−C chord vector (see Figure 4 for definition) OACF at 400 and 450 K is illustrated in Figure 4. Here the fits are quite reasonable. This illustrates a fundamental difference between the HH model and the VJGM model: no additional function is required in the VJGM model to obtain contributions from long relaxation time modes. The VJGM model, which approaches $1/t^{1/2}$ behavior at long times, appears to overestimate the contribution of very long time modes, with the OACF from simulation decaying faster than the VJGM model at very long times. This deviation may reflect the finite molecular weight of the chains, i.e., the lack of contribution from modes with relaxation times longer than the Rouse time. At very short times, the VJGM model matches the behavior of the C−C−C vector $P_1(t)$ OACF more accurately than that of the C−C vector OACF (compare the insets of Figures 3 and 4). This may be due in part to relaxation of the OACF due to librations (torsional oscillations) which are not accounted for in the VJGM model. These effects would be greater for the C−C vector than the C−C−C vector.

Finally, the $P_1(t)$ OACF for the C−H vector at 400 and 450 K are shown in Figure 5, along with fits of MKWW to the data. In contrast to the C−C vector and C−C−C chord vector, the C−H vector shows only a very minor contribution from the long-time exponential tail, as indicated in Table 3. The C−H vector OACF decays so rapidly that it cannot be fit effectively by the VJGM model.

Comparison of the τ_{tail} values from Table 3 with the Rouse times for the end-to-end vector relaxation given in Table 2 indicates that the portion of the relaxation of local bond vectors described by the single exponential term of the HH and MKWW models is due to reorientation on long time scales, comparable to the relaxation time for reorientation of the entire chain. The $P_1(t)$ OACF for the C−H vectors, which are essentially perpendicular to the local chain axis, can apparently relax almost completely by torsional transitions alone, with little dependence on larger scale reorientation. Relaxation of the $P_1(t)$ OACF for C−C vectors, in

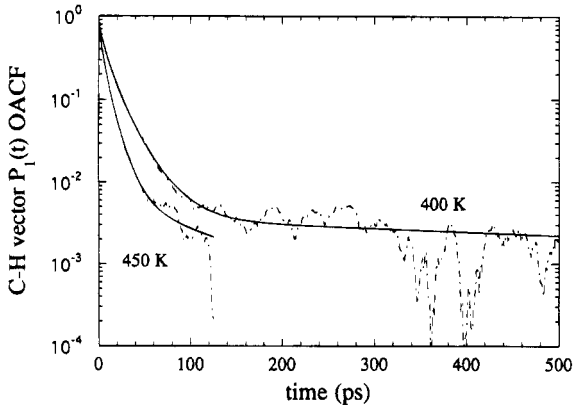

Figure 5. $P_1(t)$ OACF for the C−H vector. Simulation data are the dash−dot line. The solid lines are fits of the MKWW model.

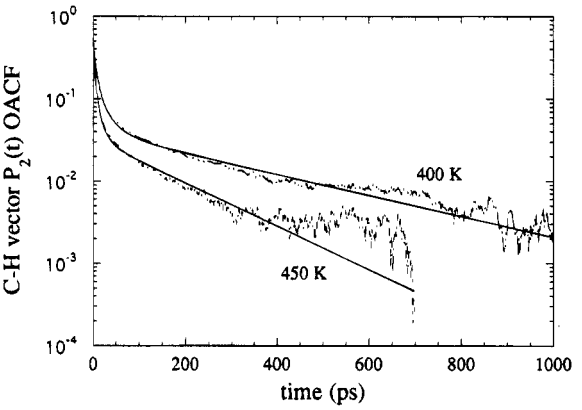

Figure 6. $P_2(t)$ OACF for the C−H vector. Simulation data are the dash−dot line. The solid lines are fits of the MKWW model.

Table 4. MKWW Model Fit Parameters for $P_2(t)$ OACF

vector	temp (K)	τ (ps)	β	A	τ_{tail} (ps)
C−H	400	2.56	0.47	0.961	341
	450	1.42	0.49	0.968	165
C−C	400	6.21	0.58	0.958	465
	450	3.23	0.61	0.959	163
C−C−C chord	400	11.00	0.48	0.886	479
	450	5.17	0.53	0.884	203

contrast, requires considerable contribution from larger scale reorientation. The contribution of the long-time component becomes even greater for the relaxation of the $P_1(t)$ autocorrelation function for C−C−C chord vectors as indicated in Table 3.

***P*₂(*t*) Autocorrelation Functions.** Experimentally measured T_1 and NOE values from ^{13}C NMR spin−lattice relaxation experiments are directly related to the $P_2(t)$ OACF for the C−H vector. The C−H vector $P_2(t)$ OACF is shown in Figure 6. It can be seen that the MKWW model fits the data reasonably well, with the greatest variation being for the long-time data at 450 K. It was found that the HH and VJGM models, which were derived for $P_1(t)$ OACF, did a poor job in fitting the $P_2(t)$ autocorrelation functions. This is illustrated in Figure 4 for the VJGM model, where it can be seen that the model does a poor job in describing the C−C−C chord vector $P_2(t)$ OACF at long times. The fit parameters for the MKWW model for the $P_2(t)$ OACF of C−H, C−C, and C−C−C chord vectors are given in Table 4. Unlike tetrahedral lattice chains,[13,15−16] the $P_1(t)$ and $P_2(t)$ OACF are far from identical, as can be seen by comparing Tables 3 and 4. The τ_{tail} values for the MKWW model shown in Table 4 are comparable to the

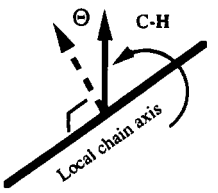

Figure 7. Schematic representation of reorientation of the C−H vector due to rotation about a local chain axis.

τ_{KWW} times for the $P_2(t)$ end-to-end vector OACF given in Table 2. A similar relationship is seen for $P_1(t)$ OACF, as discussed above.

The contributions of the single exponential to relaxation of the $P_2(t)$ functions for the C−C and C−C−C chord vectors are smaller than the contribution of the single exponential to the $P_1(t)$ functions. In contrast, the contribution is much larger for the $P_2(t)$ function than for the $P_1(t)$ function for the C−H vector, which has no significant long-time tail contribution. To understand the behavior of the C−H vector OACF, we can picture a C−H vector as perpendicular to the local chain axis, shown schematically in Figure 7. Many rotations about this axis occur from conformational transitions, resulting in reorientation of the C−H vector within a plane. The C−H vector autocorrelation functions resulting from these motions are

$$P_1(\infty) = \frac{\int_0^{2\pi} \cos\theta \, d\theta}{2\pi} = 0 \tag{11}$$

$$P_2(\infty) = \frac{1}{2}\left(\frac{3\int_0^{2\pi} \cos^2\theta \, d\theta}{2\pi} - 1\right) = \frac{1}{4} \tag{12}$$

Hence, contributions from motions of the type illustrated in Figure 7 may lead to almost complete decay of the C−H vector $P_1(t)$ OACF, accounting for the lack of a "tail" for this function, while the $P_2(t)$ OACF would show such a "tail" because the function does not decay completely from such motions. For bond vectors such as the C−C bond and C−C−C chord, which have significant components lying along the local chain backbone, the magnitude of the long-time tail component, or contribution of the long wavelength or relaxation time modes, is much greater than for the C−H vectors. The relaxation times for the tails of the C−H, C−C, and C−C−C chord vector autocorrelation functions are comparable, indicating that they arise from closely related motions. The different behaviors of the OACF for the various bond vectors, or the anisotropy of the relaxation, has been noted previously by theoretical models[15−17] and simulations.[12,15,18]

Long-Time Behavior. From the above considerations, it is apparent that the long-time behavior of the bond vector OACF reflects the contribution of long wavelength or relaxation time modes, with the exception of the C−H $P_1(t)$ OACF. de Gennes[19] showed that the Rouse model yields a long-time behavior

$$P_1(t) \propto 1/t^{1/2} \tag{13}$$

for the OACF of long chains, indicating a contribution of long wavelength modes of the chain to the reorientation of local bond vectors. The $P_1(t)$ OACF of the C−C bond and C−C−C chord vectors along with the C−C−C chord vector $P_2(t)$ are shown in Figure 8. Also shown for each OACF is a function proportional to $1/t^{1/2}$ which arbitrarily matches the OACF at 500 ps for 400 K OACF

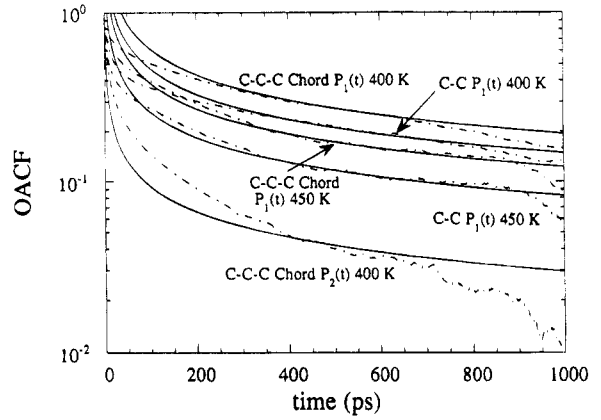

Figure 8. Representation of selected simulation OACF (dash–dot lines) with $1/t^{1/2}$ functions (solid lines) at long times.

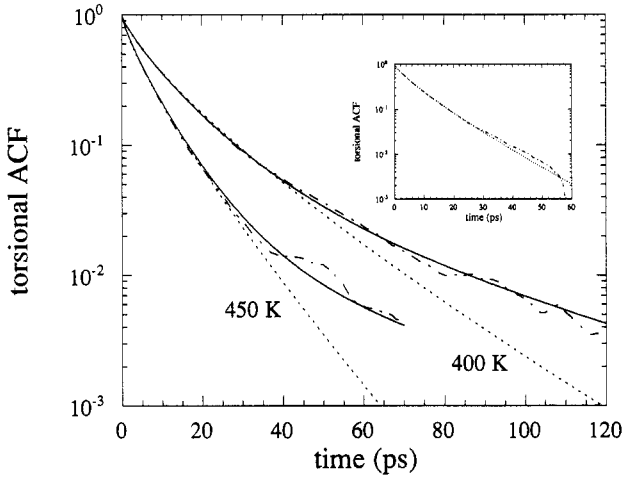

Figure 9. Torsional autocorrelation function. The dash–dot lines are the simulation data. Dotted lines are KWW fits. Solid lines are MKWW fits. The inset shows the behavior of isolated chains at 400 K.

and 400 ps for 450 K OACF. This function represents reasonably well the long-time behavior of the $P_1(t)$ OACF but not the $P_2(t)$ OACF. The deviation of the $P_1(t)$ OACF from eq 13 at longer times may reflect the finite molecular weight of the chains discussed above in conjunction with the VJGM model.

Torsional Autocorrelation Function. The torsional autocorrelation function is defined as[19]

$$P_\phi(t) = \frac{\langle \cos \phi(t) \cos \phi(0) \rangle - \langle \cos \phi(0) \rangle^2}{\langle \cos \phi(0) \cos \phi(0) \rangle - \langle \cos \phi(0) \rangle^2} \quad (14)$$

where $\phi(t)$ is the angle of a skeletal torsion and the average is over all skeletal torsions. Previously,[2] we found that $P_\phi(t)$ for n-$C_{44}H_{90}$ melts was not well fit by the KWW equation (eq 4) for values of $P_\phi(t) \leq 0.05$. This is illustrated in Figure 9, where it can also be seen that the fit to $P_\phi(t)$ is much improved when the MKWW model is utilized. The contribution of the long relaxation time single exponential to the decay of $P_\phi(t)$ was found to be somewhat greater at 400 K than at 450 K.[2] In addition, the torsional correlation time

$$\tau_\phi = \int_0^\infty P_\phi(t)\, dt \quad (15)$$

was found to have an apparent activation energy of about one $t-g$ barrier (around 3 kcal/mol) when the single exponential contribution to $P_\phi(t)$ was excluded and an apparent activation energy of 4 kcal/mol when the tail contribution was included. The single exponential contribution to $P_\phi(t)$ may become more important as the temperature decreases further and may contribute to non-Arrhenius behavior for the torsional correlation time. We are currently performing simulations of n-$C_{44}H_{90}$ at 350 K to investigate this effect. In this regard, it is of interest to note that a non-Arrhenius behavior of the torsional autocorrelation function was indicated at lower temperatures in the simulations of amorphous polymethylene by Boyd et al.[20] In that work, a single exponential was not included to describe the long-time behavior of the torsional autocorrelation functions.

Table 5. Rates of Conformational Transitions and Barrier Crossings

case	transitions	barrier crossings (per 100 ps)	ratio
400 K melt	6.2 ± 0.1	25.3 ± 0.8	0.24
400 K isolated	8.8 ± 0.2	26.4 ± 0.5	0.33

In an effort to better understand the long-time behavior of $P_\phi(t)$, we performed simulations of isolated n-$C_{44}H_{90}$ chains at 400 K. $P_\phi(t)$ for the isolated chains is shown in the inset in Figure 9, along with a KWW fit. The fit is reasonable down to $P_\phi(t) < 0.01$, where statistical uncertainties become relatively large. It is apparent from comparing $P_\phi(t)$ for the melt and isolated chains at 400 K that the presence of the melt matrix slows down the rate of decay of $P_\phi(t)$, i.e., the rate of conformational transitions. This can be seen in Table 5, where the rates of transitions and barrier crossings for melt and isolated chains are compared. While the transition rate is lower for the melt chains, the barrier crossing rates are comparable. Additionally, the isolated chain torsional ACF shows no indication of the persistent long-time component seen in the melt. This long-time component must reflect the restrictions of the melt matrix on conformational transitions, as the effect is not seen in isolated chains. Effects of local density and orientational correlations could cause some torsions to undergo transitions at a rate much slower that the average conformational transition rate. These effects would necessarily preclude complete decay of $P_\phi(t)$ on the time scale of the conformational transitions. The resulting broad distribution of relaxation times may lead to behavior for $P_\phi(t)$ which may not be well described, especially at long times, by the KWW equation. Increasing heterogeneity in conformational transition rates with decreasing temperature has been observed in simulations of polymethylene melts[20] and poly(ethylene oxide) melts.[21] Finally, it should be emphasized that the long relaxation time single exponential term in the torsional autocorrelation functions has a much shorter relaxation time than that observed for the corresponding term for the local bond vector OACF and hence reflects truly local effects.

Correlation of Conformational Transitions. Previously,[2] we performed a Hazard analysis[22] of conformational transitions in n-$C_{44}H_{90}$ melts. We found a high degree of self-correlation, second-neighbor correlation, and fourth-neighbor correlation.[2] Here we have analyzed the correlation of conformational transitions in greater detail. We look only at transitions for the central nine bonds and their neighbors in $C_{44}H_{90}$ in order to minimize end effects.

In continuing our examination of the correlation of conformational transitions in $C_{44}H_{90}$ melts, we determined the probability for each type of transition. We

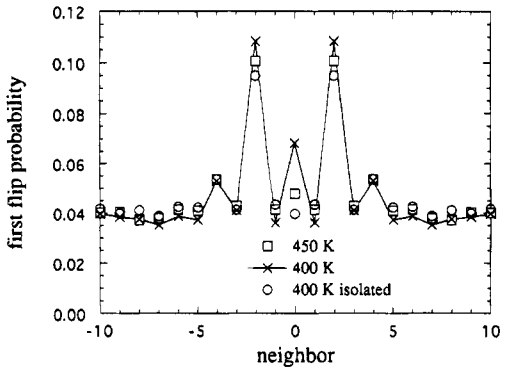

Figure 10. First flip probability for neighbors of a bond which has undergone a transition. Points at 400 K are connected by a solid line for clarity.

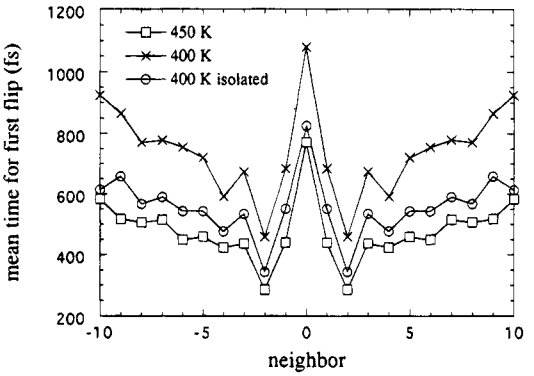

Figure 11. Mean time for occurrence of a first flip for neighbors of a bond which has undergone a transition. Points are connected by solid lines for clarity.

find that at 400 K, 97% of the transitions are $t \rightleftarrows g^{\pm}$ transitions, while only 3% are $g^{+} \rightleftarrows g^{-}$ transitions. As the latter involves crossing the higher cis barrier, the low fraction is expected. In contrast, recent simulations employing a force field with a low cis barrier found significant occurrences of cis barrier crossings.[20] Results of our ab initio studies of n-butane and n-hexane indicate that the cis barrier is considerably higher than the $t \rightleftarrows g^{\pm}$ barrier (see Table 1 and ref 4).

Correlation of Transitions. In addition to using Hazard analysis to examine correlation of conformational transitions, we have also used the following method employed by Boyd et al.[20] A transition at bond n is defined as being ith-neighbor correlated if the next transition within $n \pm 10$ bonds is at $n \pm i$. Such an analysis is presented for the central nine bonds in n-$C_{44}H_{90}$ in Figure 10. A high degree of second-neighbor correlation can be seen. This is consistent with the Hazard analysis.[2] Self-correlation and fourth-neighbor correlation above the "background" level can also be seen, although apparently to a much smaller extent than was seen in the Hazard analysis. This apparent discrepancy will be discussed below. The amount of self-correlation and second-neighbor correlation decreases with increasing temperature. For the isolated chains, the amount of second-neighbor correlation is somewhat less than seen for the melt, and the amount of self-correlation is significantly less than is seen for the melt. This latter feature appears to indicate that the self-correlation (as defined here) seen in the melts is, to a large extent, a memory effect induced by the surrounding matrix. Similar differences in self-correlation between the melt and isolated chains were seen by Boyd et al.[20] and were seen to become much more pronounced at lower temperatures.

The mean time for directly correlated flips as defined above for the neighbors of a given bond is shown in Figure 11. For all cases, the mean time for a self-flip is much longer than that for the other neighbors. This is consistent with results of the Hazard analysis,[2] where it was determined that the self-correlated transitions were not in general short-time, immediate reversals of transitions. In contrast, the mean time for second-neighbor correlated transition is much shorter than that for the other neighbors. Again, this is consistent with results of the Hazard analysis and indicates that many of the correlated second-neighbor transitions occur immediately after completion of the triggering transition, consistent with the gauche migration and gauche generation/annihilation mechanism.[22] The mean time for the fourth-neighbor correlated transitions is shorter than that for any other correlated transition except the second neighbor, indicating the possible presence of highly cooperative mechanisms like the gauche migration and gauche generation/annihilation mechanisms seen for second-neighbor cooperative transitions.

Table 6. Mechanisms of Second- and Fourth-Neighbor Correlated Transitions

system	gauche migration	gauche gen/annih	other t centered	all others
Second-Neighbor Correlated Transitions				
450 K melt	0.39	0.35	0.12	0.14
400 K melt	0.42	0.35	0.11	0.12
400 K isolated	0.39	0.33	0.12	0.16
phantom Brownian[a]	0.44	0.35	0.05	0.16
Direct Fourth-Neighbor Correlated Transitions				
450 K melt	0.22	0.23	0.13	0.42
400 K melt	0.27	0.26	0.12	0.35
400 K isolated	0.24	0.24	0.11	0.41

[a] Brownian simulation of phantom chains in ref 12 at 425 K. Transitions are considered to be correlated if they occur within τ_{cut} of each other. This definition is different from that used in this study (see text).

Second-Neighbor Correlation. We have analyzed mechanisms of second-neighbor correlated transitions in Table 6. For this purpose, a second-neighbor correlated transition is as defined above where, after a transition at bond n, the next transition within $n \pm 10$ bonds is at $n \pm 2$. Mechanisms are classified as gauche migration $g^{\pm}tt \rightleftarrows ttg^{\pm}$, gauche generation/annihilation $ttt \rightleftarrows g^{\pm}tg^{\mp}$, and other t centered, with the remaining cases classified as "all others". We find that for both melt and isolated chains, the counter rotating cranklike gauche migration and gauche generation/annihilation mechanisms account for 70–80% of the second-neighbor correlated transitions. The influence of the melt matrix on the mechanism for the second-neighbor correlated transitions is minor, as can be seen by comparing the results for 400 K melts with 400 K isolated chains. These results are also consistent with those of Brownian dynamics simulations of phantom chains by Helfand et al., who used a somewhat different definition.[12,22] The higher percentage of transitions occurring by gauche generation or migration mechanisms (77% at 400 K) in the melt than for isolated chains (72% at 400 K) may reflect restrictions on transitions due to the matrix.

Fourth-Neighbor Correlation. Hazard analysis indicates a relatively high degree of fourth-neighbor correlation in conformational transitions.[2] Fourth-neighbor correlation is indicated in Figure 10, but to a smaller degree than is indicated from Hazard analysis. In order to try to better understand fourth-neighbor correlation in conformational transitions in n-$C_{44}H_{90}$, we

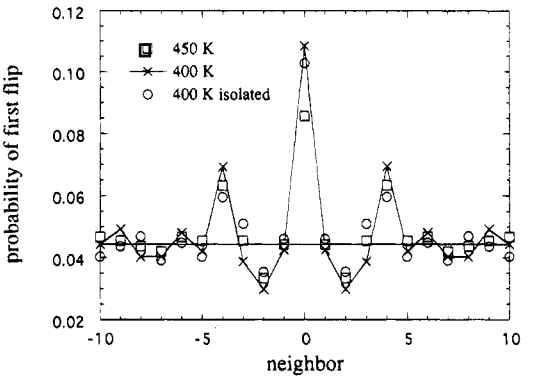

Figure 12. First flip probability for neighbors of a bond whose second neighbor has undergone a transition. The horizontal line gives the background flip rate. Points at 400 K are connected by a solid line for clarity.

further monitored transitions (as defined above) *after* a second-neighbor transition occurred. In other words, after a transition in bond n, followed by a transition in bond $n \pm 2$, we looked for the next transition within $n \pm 10$. In this analysis, no differentiation was made as to whether it is bond $n + 2$ or bond $n - 2$ which is second-neighbor correlated with bond n. These results are plotted in Figure 12. After a transition in bond $n \pm 2$, the most likely following transition is in the original bond n. However, a high degree of correlation with $n \pm 4$ is also seen. One of these is the second neighbor to the $n + 2$ or $n - 2$ bond which underwent the previous transition. If we subtract a reasonable background transition probability (indicated by the solid line) and assume no correlation between $n + 2$ and $n - 4$ or $n - 2$ and $n + 4$, the degree of correlation between $n \pm 2$ and $n \pm 4$ (given as the sum of $n + 4$ and $n - 4$ after subtracting the background) is comparable to the correlation between $n \pm 2$ and n. The implications of this are as follows: first, because the correlation of $n \pm 2$ with n is comparable to that of $n \pm 2$ with $n \pm 4$, a more or less random movement of second-neighbor correlated transitions up and down the chain is indicated; second, many of the fourth-neighbor correlated transitions seen in the Hazard plot are actually second-neighbor correlated transitions of prior second-neighbor correlated transitions. In the definition of correlation given above, once the first transition within the $n \pm 10$ neighbors occurs, the clock is turned off until there is another transition in bond n. In the Hazard analysis, all transitions of neighbors are recorded until bond n itself undergoes a transition. In other words, many of the fourth-neighbor correlated transitions seen in the Harard analysis are associated with second-neighbor correlated transitions. This also explains the intermediate behavior between self-correlated and second-neighbor correlated transitions seen for fourth-neighbor transitions in the Hazard analysis in terms of "correlation time". Some of the fourth-neighbor correlated transitions occur essentially immediately after the original transition in bond n, as was found for second-neighbor transitions (see Figure 11). Some of the fourth-neighbor correlated transitions follow prior second-neighbor transitions (and show up only in Figure 12 and the Hazard analysis) and occur at a significantly later time after the transition in bond n than "direct" fourth-neighbor transitions.

As discussed above, some "direct" fourth-neighbor correlated transitions occur. We have analyzed the mechanisms of these transitions as we did for second-neighbor correlated transitions. Here, a gauche migration is defined as $g^{\pm}t\phi tt \rightleftharpoons tt\phi tg^{\pm}$, gauche generation/annihilation as $tt\phi tt \rightleftharpoons g^{\pm}t\phi tg^{\mp}$, and other t centered when bonds 2 and 4 are trans but the mechanism is not gauche generation/annihilation or migration. The remaining cases are classified as "all other". The central bond (ϕ) can be trans or gauche. The gauche generation/annihilation and migration mechanisms as defined above are counter rotating "cranklike" mechanisms analogous to those for second-neighbor cooperative transitions. Table 6 shows the detailed distribution of various direct fourth-neighbor correlated transitions. Although not as dominant as in second-neighbor cooperative transitions, gauche migration and gauche generation/annihilation mechanisms in fourth-neighbor cooperative transitions still remain important.

Conclusions

Our simulations for n-$C_{44}H_{90}$ melts, using an explicit atom model, yield self-diffusion coefficients which agree with experimental values to within about 20%. The monomer friction constants from self-diffusion coefficients are considerably smaller than estimates from the Rouse model fit of the end-to-end chain vector reorientation and experimental melt viscosities, reflecting the fact that these chains are not long enough to assume Gaussian coils.

The local bond vector OACF, with the exception of the C−H $P_1(t)$ OACF, exhibit important contributions from long relaxation time modes, yielding a long-time tail in the OACF. The degree to which these long-time motions are required to bring about relaxation of the local bond vectors is a function of which local bond axes are involved and the order of the autocorrelation function being considered, and results in considerable anisotropy in the relaxation. However, the "relaxation time" of the tail is similar for all the bond vectors and is comparable to the Rouse time of the chains.

The relaxation time for the apparent long-time component of the torsional autocorrelation functions is much shorter than that for the local chain vectors (i.e., the Rouse time), reflecting what we consider to be a truly local effect of dynamic heterogeneity. Comparison of the torsional autocorrelation function for melt chains with that for isolated chains indicates that the long-time persistence of the torsional ACF in the melt is due to matrix restrictions on conformational transitions. These restrictions may be the result of local density or orientation correlation effects which leads to considerable heterogeneity in conformational transition rates.

Correlated conformational transitions are prominent for the self, second, and fourth neighbors. The direct self-correlated transitions, which are nearly absent for isolated chains, become more important in melt chains with decreasing temperature. These transitions are not immediate reversals although they arise from the constraints of the melt matrix. The direct second- and fourth-neighbor correlated transitions are primarily gauche migration and gauche generation/annihilation type transitions. Moreover, the second-neighbor correlated transitions appear to propagate more or less randomly along the chain, contributing to the self-correlated and fourth-neighbor correlated transitions seen in the Hazard analysis.[2]

In examining conformational dynamics in melt chains, it is apparent that much of the physics of chains in the condensed phase comes from chain connectivity and intrinsic internal conformational characteristics. This can be seen by comparing melt simulations with simulations of isolated chains and stochastic dynamics simu-

lations, where qualitatively similar behavior is often seen. There are also, however, differences between both long-time and local dynamics of melt and isolated or solution chains, which become greater with decreasing temperature. As conformational dynamics determine the long-time and local dynamics of polymer chains, difference in long-time and local dynamics between chains in the melt and solution must be reflected in differences in conformational dynamics. This subject will be considered in future publications.

Acknowledgment. G.D.S. is grateful for support provided by NASA through Eloret Contract NAS2-14031. The authors also wish to thank Dr. Wolfgang Paul for helpful discussions.

References and Notes

(1) Current address: Department of Chemical Engineering, W2030 Engineering Bldg. East, University of Missouri—Columbia, Columbia, MO 65211.
(2) Smith, G. D.; Yoon, D. Y.; Zhu, W.; Ediger, M. D. *Macromolecules* **1994**, *27*, 5563.
(3) Smith, G. D.; Yoon, D. Y. *J. Chem. Phys.* **1994**, *100*, 649.
(4) Smith, G. D.; Jaffe, R. L., in preparation. A survey of experimental and quantum chemistry values for conformational energies and barriers in n-alkanes will be included.
(5) Dunning, T. H. *J. Chem. Phys.* **1989**, *90*, 1007.
(6) Raghavarchari, K.; Trucks, G. W.; Pople, J. A.; Head-Gordon, M. *Chem. Phys. Lett.* **1989**, *157*, 479.
(7) Doi, M.; Edwards, S. F. *The Theory of Polymer Dynamics*; Clarendon Press: Oxford, 1986.
(8) Pearson, D. S.; Ver Strate, G.; von Meerwall, E.; Schilling, F. C. *Macromolecules* **1987**, *20*, 1133. Pearson, D. S.; Fetters, L. J.; Graessley, W. W.; Ver Strate, G.; von Meerwall, E. *Macromolecules* **1994**, *27*, 711.
(9) Yoon, D. Y.; Flory, P. J. *J. Chem. Phys.* **1974**, *61*, 5366.
(10) Paul, W.; Yoon, D. Y.; Smith, G. D., in preparation.
(11) Hall, C. K.; Helfand, E. *J. Chem. Phys.* **1982**, *77*, 3275.
(12) Weber, T. A.; Helfand, E. *J. Phys. Chem.* **1983**, *87*, 2881.
(13) Valeur, B.; Jarry, J. P.; Geny, F.; Monnerie, L. *J. Polym. Sci., Polym. Phys. Ed.* **1975**, *13*, 667, 675.
(14) Dejean de la Batie, R.; Laupretre, F.; Monnerie, L. *Macromolecules* **1988**, *21*, 2045.
(15) Gotlib, Y. Y.; Darinskii, A. A.; Neelov, I. M.; Torchinskii, I. A.; Shevelev, V. A. *Polym. Sci. USSR (Engl. Transl.)* **1992**, *34*, 842.
(16) Gotlib, Y. Y.; Torchinski, I. A.; Shevelev, V. A. *Makromol. Chem., Theory Simul.* **1993**, *2*, 13.
(17) Bahar, I.; Erman, B. *J. Chem. Phys.* **1988**, *88*, 1228.
(18) Takeuchi, H.; Roe, R. J. *J. Chem. Phys.* **1991**, *94*, 7446.
(19) de Gennes, P.-G. *Physics (Long Island City, N.Y.)* **1967**, *3*, 37.
(20) Boyd, R. H.; Gee, R. H.; Han, J.; Jin, Y. *J. Chem. Phys.* **1994**, *101*, 788.
(21) Smith, G. D.; Jaffe, R. L.; Yoon, D. Y., in preparation.
(22) Helfand, E.; Wasserman, Z. R.; Weber, T. A. *Macromolecules* **1980**, *13*, 526.

MA9463270